

IC 4406: a radio-infrared view

Luciano Cerrigone^{1,2} and Joseph L. Hora¹

Harvard-Smithsonian Center for Astrophysics, Cambridge, MA 02138 USA

University of Catania, Catania, Italy

Grazia Umana³ and Corrado Trigilio³

INAF, Catania Astrophysical Observatory, Catania, Italy

ABSTRACT

IC 4406 is a large (about $100'' \times 30''$) southern bipolar planetary nebula, composed of two elongated lobes extending from a bright central region, where there is evidence for the presence of a large torus of gas and dust. We show new observations of this source performed with IRAC (Spitzer Space Telescope) and the Australia Telescope Compact Array. The radio maps show that the flux from the ionized gas is concentrated in the bright central region and originates in an intricate structure previously observed in $H\alpha$, while in the infrared images filaments and clumps can be seen in the extended nebular envelope, the central region showing toroidal emission. Modelling of the infrared emission leads to the conclusion that several dust components are present in the nebula.

Subject headings: Radio continuum: stars, Infrared: stars, Planetary nebulae: individual (IC 4406)

1. Introduction

IC 4406 is a well-studied southern planetary nebula. It has been imaged with several telescopes at different wavelength ranges. Near-IR images show two H_2 lobes (Storey 1984), orthogonal to the nebula's major axis and $\sim 25''$ away from each other. These peaks are approximately coincident with the two blobs observed in $H\alpha + [N\ II]$ and $[O\ III]$ (Sahai et al. 1991), interpreted as indicative of the presence of a dense equatorial torus of dust. The optical images show a central ionized region about $32''$ in diameter. CO maps show the presence of a collimated high velocity outflow in the polar direction and with $[CO]/[H_2] \approx 5 \times 10^{-6}$ and a total molecular mass in the range $0.16\text{--}3.2\ M_\odot$ (Sahai et al. 1991). Hubble Space Telescope

(HST) WFPC2 images in [N II], H α and [O III] have revealed the existence of an intricate system of dark lane features, which led to the name of “Retina Nebula” for this object (O’Dell et al. 2002). The nebula appears to be chemically homogeneous, as Corradi et al. (1997) found no evidence of radial variation for He, O, N, Ne, and Ar. Cox et al. (1992) have detected several C-rich features at mm wavelengths, such as CN, HCO⁺, HCN and HNC, which indicate the nebula is C-rich, although a C/O ratio of 0.6 is reported by Cohen & Barlow (2005).

IC 4406 is a relatively low electron density nebula. Values in the 400-2000 cm⁻³ range have been estimated using several different optical and infrared lines, with values derived by [S II] and [O III] doublets matching around 540 cm⁻³ (Liu et al. 2001; Wang et al. 2004). Its central star has a He II Zanstra temperature of 96800 K (Phillips 2003) and its distance is probably around 1.6 kpc (Sahai et al. 1991), although some authors claim it may be well overestimated (O’Dell et al. 2002).

Gruenwald et al. (1997) have modeled IC 4406 with a 3-D photoionization code and fit many observed line intensities assuming there is a torus around the central star. They find as a best fit a central star temperature of 8×10^4 K, luminosity of 400 L_⊙, torus density 1500 cm⁻³ and nebular density 100 cm⁻³.

In general, comparisons of IR images of planetary nebulae, which trace the molecular gas and warm dust emission, to optical line images, which trace the ionized gas, have shown the presence of similar structures (Latter et al. 1997), leading to the conclusion that molecular and ionized gas spatially coexist in planetary nebulae, as well as dust grains, despite the different physical conditions these components are presumed to survive in. We have observed IC 4406 in the radio range to inspect the distribution of the ionized gas in its envelope and in the infrared to check for emission from the equatorial dust and molecular gas.

In §2 we explain how we performed our observations and reduced the data; in §3 we show our results and in particular in §3.1 how we modeled the emission in the radio and infrared ranges; §3.2 compares our model results to the nebular parameter values obtained directly from the observational data; in §4 we summarize the present work.

2. Observations and Data reduction

Radio observations were performed at the **Australia Telescope Compact Array** (ATCA)¹ on November 24, 2005 (17:00:00–08:00:00 UT) and December 11, 2005 (15:30:00–02:00:00 UT), simultaneously at 4.8 and 8.6 GHz. The November run was performed with the array in 1.5C configuration, while for the December one the configuration was 6.0A. The adopted configurations are both linear but with different antenna positions giving maximum baselines of 4500 m (1.5C) and 5939 m (6.0A), minimum baselines of 77 m (1.5C) and 337 m (6.0A). The pre-calibration of the array was performed observing 0823-500, while the absolute flux calibrator was 1934-638. Another target was also observed during our two runs and the total on-target time was about 7 hours for each of the two. The phase calibrator chosen for IC 4406 was 1431-48, which is 4.76° away from the target. The data were reduced with **MIRIAD**, following a standard reduction procedure as recommended in the MIRIAD User’s Guide. The data from the two runs were combined into one dataset, obtaining a uv coverage from 0.9 to 96 k λ at 4.8 GHz and from 1.5 to 172 k λ at 8.6 GHz. These correspond to an angular resolution of $2.2''$ at 4.8 GHz and $1.2''$ at 8.6 GHz, while the largest observable structures (Largest Angular Scale) are $230''$ and $140''$ respectively. Such a setup suits the need to collect all the radiation from the target, whose maximum size, as previously mentioned, is about $100''$.

As at both frequencies our target appears to be quite resolved, the estimate of its flux has been performed on maps obtained using tapering (task INVERT: fwhm=15, for both frequency bands). This results in larger weights for the visibility points corresponding to short baselines, then limits the chance to miss extended flux in the final map, although possibly producing higher noise. Since the error in our measurement is primarily determined by the error in the absolute flux calibration, tapering is not an issue. With such procedure we measure at 4.8 GHz 103.3 ± 0.3 mJy and 92.5 ± 0.4 mJy at 8.6 GHz, which, taking into account a typical 5% error in the absolute calibration, gives us the following final measurements: 103 ± 5 mJy at 4.8 GHz and 92 ± 5 mJy at 8.6 GHz².

Infrared observations were performed with the **InfraRed Array Camera** (IRAC) (Fazio et al. 2004) onboard the Spitzer Space Telescope (Spitzer) at 3.6, 4.5, 5.8 and 8.0 μ m on March 06, 2004 (UT 09:54:16.311) as part of the GTO program “Studying stellar ejecta on the large scale with SIRTf-IRAC”. Six High Dynamic Range 30 sec dithered frames were obtained at

¹The Australia Telescope Compact Array is part of the Australia Telescope which is funded by the Commonwealth of Australia for operation as a National Facility managed by CSIRO.

²The final error has been estimated as $\sigma = \sqrt{rms^2 + (\sigma_{cal}F)^2}$, where σ_{cal} is the 5% relative error in absolute calibration and F is the measured flux density.

each wavelength, for a total exposure time of 180 sec per channel.

Basic Calibration Data were retrieved from Spitzer archive, cleaned to correct such artifacts as mux-bleeding and banding and then coadded using **IRACproc** (Schuster et al. 2006). For flux measurement the images were first converted from MJy/sr (IRAC BCD files are in units of MJy/sr) into Jy units using IRACproc. Then in each image four areas were boxed with a polygon using the task CGCURS in MIRIAD, the mean emission in each polygon was calculated then averaged to obtain an estimate of the background. The standard deviation of the background mean value was assumed as an error. The whole nebula in each image was then boxed with a polygon of approximately $135'' \times 65''$. The size of the emitting nebula has been determined as the contour at the background+ 3σ level and is approximately: at $3.6 \mu\text{m}$ $110'' \times 45''$, at $4.5 \mu\text{m}$ $120'' \times 50''$, at $5.8 \mu\text{m}$ $120'' \times 60''$ and at $8.0 \mu\text{m}$ $125'' \times 65''$. The flux within each $135'' \times 65''$ polygon was summed up and the same procedure was adopted for the field star observed West of the central core, so that its flux was subtracted to the overall nebula's one. The result was corrected for extended emission according to the IRAC Data Handbook for aperture photometry. The error in the background estimate was assumed as the error of the flux measurement. We have measured at 3.6 , 4.5 , 5.8 , and $8.0 \mu\text{m}$ the following fluxes respectively: 64 ± 2 , 101 ± 4 , 122 ± 7 , and 248 ± 8 mJy.

Tab.1 and Tab.2 summarize the pointing coordinates and results of our radio and infrared observations.

3. Results and Analysis

Our radio maps (Fig.1) show the presence of a $42'' \times 56''$ (3σ level) emitting region at 4.8 GHz, elongated in E-W direction; at a 10% of the peak level the size of the emitting region is restricted to $32'' \times 32''$. At 8.6 GHz the 10% of the peak level gives a size of $36'' \times 40''$, in agreement with its 3σ level size.

The maps do not show any N-S blobs of emission. What is seen is a very intricate system of emitting lanes (Fig.2), which resembles what is observed by HST in H α (O'Dell et al. 2002).

Using the fluxes that we estimate at the two frequencies, we can calculate a spectral index $\alpha = -0.19 \pm 0.09$, which matches the expected value of -0.1 for an optically thin radio shell.

Fig.3 shows IRAC images of the central equatorial area of the nebula. They were plotted

with a linear scale having the peak flux and 50% of it as thresholds. Channel 1 and especially Channel 3 resemble the H_2 emission image in Storey (1984) and this is probably because the $\nu = 0-0 \text{ S}(7)$ line at $5.51 \mu\text{m}$ falls within the $5.8 \mu\text{m}$ band and several H_2 lines may contribute to the $3.6 \mu\text{m}$ image (Hora et al. 2004). Channel 4 clearly shows the emission from the torus of dust surrounding the central star. Its size is about $28'' \times 20''$, elongated in N-S direction and the angular distance between its peaks is about $14''$ (the north peak is found at $14^{\text{h}}22^{\text{m}}26^{\text{s}}.05$, $-44^{\circ}08'54''.64$ and the south one at $14^{\text{h}}22^{\text{m}}26^{\text{s}}.31$, $-44^{\circ}09'08''.14$, with a position angle of $168^{\circ}.7$). The overall size of the torus matches the approximate size of the nebula in the N-S direction ($\sim 30''$), although its peaks are much closer to the center than the H_2 blobs reported by Storey (1984), whose separation can be roughly estimated as $\sim 25''$. This indicates that the torus is partly shielding the molecular gas from the UV radiation from the central star.

Fig.4 is a combination of IRAC channels plotted with linear scale. Despite the lower resolution compared to Hubble images, IRAC is able to detect the faint emission from the neutral components in the envelope and reveals the structure of the elongated lobes. The IRAC images show filaments at different distances and inclinations from the central star, connected to the mass loss history of the nebula. The filaments that are angularly closer to the central star show relatively stronger blue ($3.6 \mu\text{m}$) emission, which may imply a higher temperature, being intrinsically closer to the central object. The overall structure observed in the envelope corresponds to the assumption that the central torus is the main collimating agent.

3.1. The Spectral Energy Distribution of IC 4406

To inspect the dust properties of our target we have collected literature data which, along with our observations, enable us to build the SED. We have retrieved 2MASS (Skrutskie et al 2006) images (J, H and Ks) from the 2MASS archive to measure our target's flux in such bands: the values in the Point Source Catalog neglect the emission from the extended envelope. To estimate the flux and its error a procedure analogous to that used for IRAC data was applied. In each image four areas were boxed with a polygon, then the mean emission in each polygon was calculated, averaged to obtain the background and its standard deviation was taken as the flux density error for the selected image. The nebula itself was boxed with a polygon around its background+ 3σ contour, the flux within the polygon was calculated then background subtracted (the polygon size was the same as for the IRAC data). 2MASS fluxes were then converted into UKIRT system J, H and K magnitudes, so that color correction according to Schlegel et al. (1998) could be performed, adopting

$E(B-V)=0.19$ (Gathier & Pottasch 1988). The IRAS color corrected data were taken from Sahai et al. (1991). In our modeling we have assumed a central star temperature of 96800 K (Phillips 2003), a distance of 1.6 kpc, and a luminosity of $170 L_{\odot}$ (Sahai et al. 1991).

We have modeled the SED separately for the radio (ATCA and single dish literature data) and infrared (IRAS, IRAC, 2MASS) emission. The radio data collected from the literature are listed in Tab.3 with their references. For the former we have solved the radiation transfer equation in a sphere having as best fitting parameters a radius of $24''$, a constant density of 450 cm^{-3} and electron gas temperature 10^4 K . This gives us an optically thin spectrum down to 800 MHz, which confirms the status of our target as a fairly evolved object, and it also provides us with an estimate of the ionized gas mass of about $0.29 M_{\odot}$. To estimate the free-free contribution from radio to near-IR wavelengths, in our model we have calculated the Gaunt factor according to Karzas & Latter (1961).

For the infrared range we have used the code DUSTY (Ivezić et al. 1999) to solve the radiation transfer, assuming once again the nebula to be spherical. DUSTY does not allow the simultaneous treatment of more than one shell, yet its output can be used as an input in a second run, thus mimicing the shell structure of the nebula.

One constraint to our model is the optical depth at a specified wavelength, which we can calculate as

$$\tau_{\nu} = 2.03 \times 10^{10} \frac{F_{\nu}}{\theta^2 B_{\nu}(T_d)} \quad (1)$$

where T_d is the dust temperature, θ the angular radius of the nebula in arcsec, F_{ν} the flux density at the frequency ν in $\text{erg cm}^{-2} \text{ s}^{-1} \text{ Hz}^{-1}$, $B_{\nu}(T_d)$ the Planck function at the temperature T_d in $\text{erg cm}^{-2} \text{ s}^{-1} \text{ Hz}^{-1} \text{ sr}^{-1}$ (Gathier et al. 1986).

The first attempts to fit the data were done with a standard MRN (Mathis et al. 1977) size distribution of the grains, with $a_{min} = 0.005$, $a_{max} = 0.26$, $n(a) \propto a^q$, $q = -3.5$, density distribution in the shell as r^{-2} , r being the shell radius, a chemical composition of amorphous Carbon only and 0.1 as optical depth at $0.55 \mu\text{m}$. The choice of an am-C only chemistry is due to the detection of several C-rich features mentioned in Section 1.

By a first inspection of the observed data points, it was evident that the data could not be matched by a single dust component. In order to fit several components, we have performed our fit in steps, fitting first the lower wavelength data in a DUSTY run reproducing a hot inner shell, then giving the output of this run as an input to a second run of DUSTY. We have been able to reproduce the observed data assuming the dust envelope is made up of three shells, containing hot, warm and cold dust. The temperature of the cold component thus obtained was used in Eq.1 to calculate τ at $60 \mu\text{m}$. We chose this wavelength because at this wavelength all the flux seems to be due to one emitting component and cirrus contribution

is negligible, which is not necessarily true at $100\ \mu\text{m}$. Having calculated the optical depth at $60\ \mu\text{m}$ with Eq.1, we checked if this value matched the one given by DUSTY in its output. This was not the case. Then we used the τ_{60} estimate as an input optical depth in DUSTY. This led to mismatch all the longer wavelength data points. We started changing the cold dust temperature, looking for a combination of T_d and τ_{60} that would allow to match the data. We found that it was not possible to reach such a match with the specified set of input parameters, the DUSTY fluxes at larger wavelengths being larger than the observed ones. We have then tried to change the density distribution dependence on the radius: such exponents as -3, -1, -0.5 were tested but none resulted into a good match to the observations. Our second attempt was changing the grain size: we noticed that the presence of larger grains in the model (up to $6.5\ \mu\text{m}$) could effectively modify the reproduced data.

Since DUSTY makes use of spherical geometry, we have assumed an effective radius of $45''$, corresponding to the radius of a circle having the same area as the dust ellipse observed in our IRAC images. The shell relative thickness parameter in DUSTY has been calculated to reproduce this angular size. The final set of parameters for our best fit is reported in Tab.4.

Fig.5 and Fig.6 show respectively the fit to the observational data points in the infrared region and the combination of the infrared and radio fits.

We notice that, if in our free-free model we had used the usual radio approximation of the Gaunt factor, the model would predict around $2\ \mu\text{m}$ a lower level of emission than observed (as can be seen in Figure 5, where the single emitting components are plotted), which might be interpreted as due to a fourth hotter component of dust missing in the model. Our proper estimate of the Gaunt factor shows how the free-free contribution in the near-IR is actually non negligible and allows us to achieve a good fit to the data points in this range. The fairly larger flux measured in K band can be explained when considering that H_2 emission has been detected in IC 4406 (Storey 1984) and several lines may fall within the K band filters, along with ionized gas lines such as $\text{Br}\gamma$. In fact Phillips & Ramos-Larios (2005) and Ramos-Larios et al. (2006) have explained the excess in Ks band in terms of H_2 emission, in particular the latter show how the Ks band 2MASS image matches the H_2 image in Storey (1984).

3.2. Nebular parameters

Our models enable us to estimate such nebular parameters as electron density, ionized gas mass and dust mass. The dust mass can be calculated from the DUSTY output following

Sarkar & Sahai (2006) as

$$M_d = 4\pi R^2 Y \frac{\tau_{100}}{k_{100}} \quad (2)$$

where R is the inner radius of the emitting shell in cm, Y is the thickness of the shell relative to R , τ_{100} and k_{100} the optical depth and absorption coefficient at $100 \mu\text{m}$. We can now use our DUSTY output for R and τ_{100} , which, for the 57 K more external shell, are estimated as $3.6 \times 10^{16} \text{ cm}$ and 2.34×10^{-5} ; Y is 30 and $k_{100} = 92 \text{ cm}^2 \text{ g}^{-1}$, calculated following Jura (1986). We thus obtain a dust mass of $6 \times 10^{-5} M_\odot$. Our radio model gives instead an average electron density of 450 cm^{-3} and ionized mass of $0.29 M_\odot$, as mentioned in the previous section.

These values can be compared to those derived by equations that directly use the observed fluxes. From our radio observations it is possible to derive the H_β flux and electron density, which can then be used to estimate the ionized mass of the nebula.

$$H_\beta = \frac{S_{4.8 \text{ GHz}}}{2.83 \times 10^9 t^{0.53} [1 + (1-x)y + 3.7xy]} \text{ erg cm}^{-2} \text{ s}^{-1} \quad (3)$$

$$n_e = 2.74 \times 10^4 \sqrt{\frac{t^{0.88} H_\beta}{\epsilon \theta^3 d}} \text{ cm}^{-3} \quad (4)$$

$$M_{ion} = \frac{11.06 d^2 t^{0.88}}{n_e} H_\beta M_\odot \quad (5)$$

In Eq.5 H_β is the H_β line flux in units of $10^{-11} \text{ erg cm}^{-2} \text{ s}^{-1}$, n_e the electron density in cm^{-3} , t the electron gas temperature in units of 10^4 K , d the distance to the star in kpc. In Eq.4 H_β is like in the previous equation, θ is the ionized gas radius as deduced from the 4.8 GHz radio map (we have used a value of $24''$) in arcsec, ϵ is the filling factor, for which we have used an average value of 0.6, t as before. In Eq.3, $S_{4.8 \text{ GHz}}$ is the 4.8 GHz flux density in Jy, t as before, x is $He^{++}/He = 0.121$, y is $He/H = 0.132$, calculated from the abundances in Corradi et al. (1997). Eq.3, 5 and 4 are from Pottasch (1984). We find $0.21 M_\odot$, 418 cm^{-3} and $3.09 \times 10^{-11} \text{ erg cm}^{-2} \text{ s}^{-1}$ for the ionized mass, electron density and H_β flux respectively, which closely match our radio model's results.

The dust mass can be estimated according to Pottasch et al. (1984) as

$$M_{dust} = \frac{4}{3} \frac{a \rho}{Q_\nu} \frac{d^2 F_\nu}{B(\nu, T_{dust})} g \quad (6)$$

Following Jura (1986), we consider 1.1 as a representative value of the power-law distribution of the emissivity of carbon grains in the infrared. We can thus calculate the dust

emissivity at $60\ \mu\text{m}$ assuming average grain radius $a = 10^{-5}\ \text{cm}$ and density $\rho = 3\ \text{g cm}^{-3}$, which results into $Q_{60} = 1.107 \times 10^{-3}$. Considering the flux at $60\ \mu\text{m}$ as due only to the cold component at $57\ \text{K}$ in our best fit, we calculate a dust mass of about $2.8 \times 10^{-4}\ \text{M}_{\odot}$. We also calculated the dust mass of the other emitting components in our fit, but they resulted to be negligible when compared to the cold dust: we find for the $700\ \text{K}$ component $5 \times 10^{-11}\ \text{M}_{\odot}$ (calculated using the $4.5\ \mu\text{m}$ flux) and for the $200\ \text{K}$ component $4 \times 10^{-8}\ \text{M}_{\odot}$ (using the $12\ \mu\text{m}$ flux). The dust to gas mass ratio can be estimated as $M_d/M_g = 1.3 \times 10^{-3}$. See Tab.5 for a summary of the parameters we have derived.

We notice that the cold dust mass value we estimate by DUSTY is one order of magnitude smaller than that calculated with Eq.6. This could perhaps be due to the approximations intrinsic to both the DUSTY modeling and the derivation of Eq.6 (i.e., spherical shape, single component chemistry, physical knowledge of dust opacity). For example, Sarkar & Sahai (2006) noticed how in general the DUSTY SEDs are not very sensitive to cooler dust at large radii, as demonstrated by the fact that large differences in shell relative thickness values do not determine drastically different SEDs. Therefore it is possible that the code itself is underestimating the amount of dust.

4. Summary

We have observed IC 4406 in the cm and 3–10 micron ranges. Our radio observations have confirmed the presence of the complicated maze of lanes already observed in $\text{H}\alpha$ in the central region of the nebula and have enabled us to calculate several nebular parameters, whose values match the classification for this target as an evolved planetary nebula, in particular its low dust to gas mass ratio and density. IRAC imaging has revealed the presence of filaments in the nebula that were not detected in previous observations.

Our IRAC measurements, combined with literature data at longer and shorter wavelengths, have enabled us to study the SED of the PN IC 4406 and reproduce it with DUSTY. This has revealed that three different dust components are needed to model the data, with temperatures ranging from 57 to $700\ \text{K}$. It has also been necessary to include in the model slightly larger grains than in the standard MRN composition (up to $6.5\ \mu\text{m}$) to account for the calculated $60\ \mu\text{m}$ optical depth. The main limits of our modeled curve are the spherical geometry assumed in DUSTY and the lack of data in the mm and sub-mm ranges, which would give a constraint on the slope of the curve. As we have observed during our trials with DUSTY, the slope of the SED in the sub-mm range changes with the maximum size of the grains included in the model. Unfortunately, in this range observations are available only for a few stars so far: none for our target.

We can speculate that in such a diversified dust environment, as we find in IC 4406, further lower temperature components may exist and future high sensitivity, high angular resolution observations will give a fundamental contribution to understand the physics of circumstellar envelopes in planetary nebulae.

L. Cerrigone acknowledges funding from the Smithsonian Astrophysical Observatory through the SAO Predoctoral Fellowship Program. This work is based in part on observations made with the Spitzer Space Telescope, operated by Jet Propulsion Laboratory under NASA contract 1407. This publication makes use of data products from the Two Micron All Sky Survey, which is a joint project of the University of Massachusetts and the Infrared Processing and Analysis Center/California Institute of Technology, funded by the National Aeronautics and Space Administration and the National Science Foundation.

Facilities: ATCA, Spitzer (IRAC)

Table 1: IC 4406 coordinates.

	<i>RA</i>	<i>DEC</i>
Spitzer	(J2000)	
IC 4406	$14^h22^m27.66^s$	$-44^\circ09'00''.0$
ATCA		
IC 4406	$14^h22^m26.28^s$	$-44^\circ09'00''.0$
1431-48 ^a	$14^h35^m16.80^s$	$-48^\circ21'47''.76$

^aPhase calibrator.

Table 2: IC 4406 measured fluxes.

Spitzer	$3.6 \mu m$	$4.5 \mu m$	$5.8 \mu m$	$8.0 \mu m$
	(mJy)	(mJy)	(mJy)	(mJy)
IC 4406	64 ± 2	101 ± 4	122 ± 7	248 ± 8
ATCA	$4.8 GHz$		$8.6 GHz$	
	(mJy)		(mJy)	
IC 4406	103.3 ± 0.3		92.5 ± 0.4	
1431-48	1020 ± 1		650 ± 1	

Table 3: IC 4406 radio fluxes from the literature.

ν (GHz)	S_ν (mJy)
0.843	104 ± 3 ^a
2.7	150 ± 60 ^b
5	110 ± 15 ^c
14.7	84 ± 8 ^d

^aMauch et al. (2003)

^bMilne & Webster (1979)

^cMilne & Aller (1975)

^dMilne & Aller (1982)

Table 4: DUSTY fit parameters.

<i>Parameters</i>	<i>Values</i>
Chemistry	100% amorphous Carbon
Central source	Blackbody at 96800 K
Density distribution	$\propto r^{-2}$
Grain size distribution	$\propto r^{-3.5}$, $a_{min} = 0.005 \mu m$, $a_{max} = 6.5 \mu m$
Hot component	$T_d = 700$ K, $\tau_{60} = 4.5 \times 10^{-6}$, $R_{in} = 7.17 \times 10^{13}$ cm, Y=14790
Warm component	$T_d = 200$ K, $\tau_{60} = 1.0 \times 10^{-5}$, $R_{in} = 1.40 \times 10^{15}$ cm, Y=750
Cold component	$T_d = 57$ K, $\tau_{60} = 6.8 \times 10^{-5}$, $R_{in} = 3.62 \times 10^{16}$ cm, Y=30

Note. — Y is the shell thickness relative to the inner radius, which is determined by the code as the layer having temperature T_d ; R_{in} is the distance to the central star of the layer having temperature T_d ; τ_{60} is the optical depth at $60 \mu m$.

Table 5: Calculated nebular parameters.

	Empirical	Models
M_{ion} (M_{\odot})	0.21	0.29
M_{dust} ($10^{-4} M_{\odot}$)	2.8	0.6
M_{dust}/M_{ion} (10^{-4})	13	2
Gas density (cm^{-3})	418	450

Note. — As “Empirical” we mean values calculated with the equations in §3.2 and with “Models” those deduced from the modeling explained in §3.1.

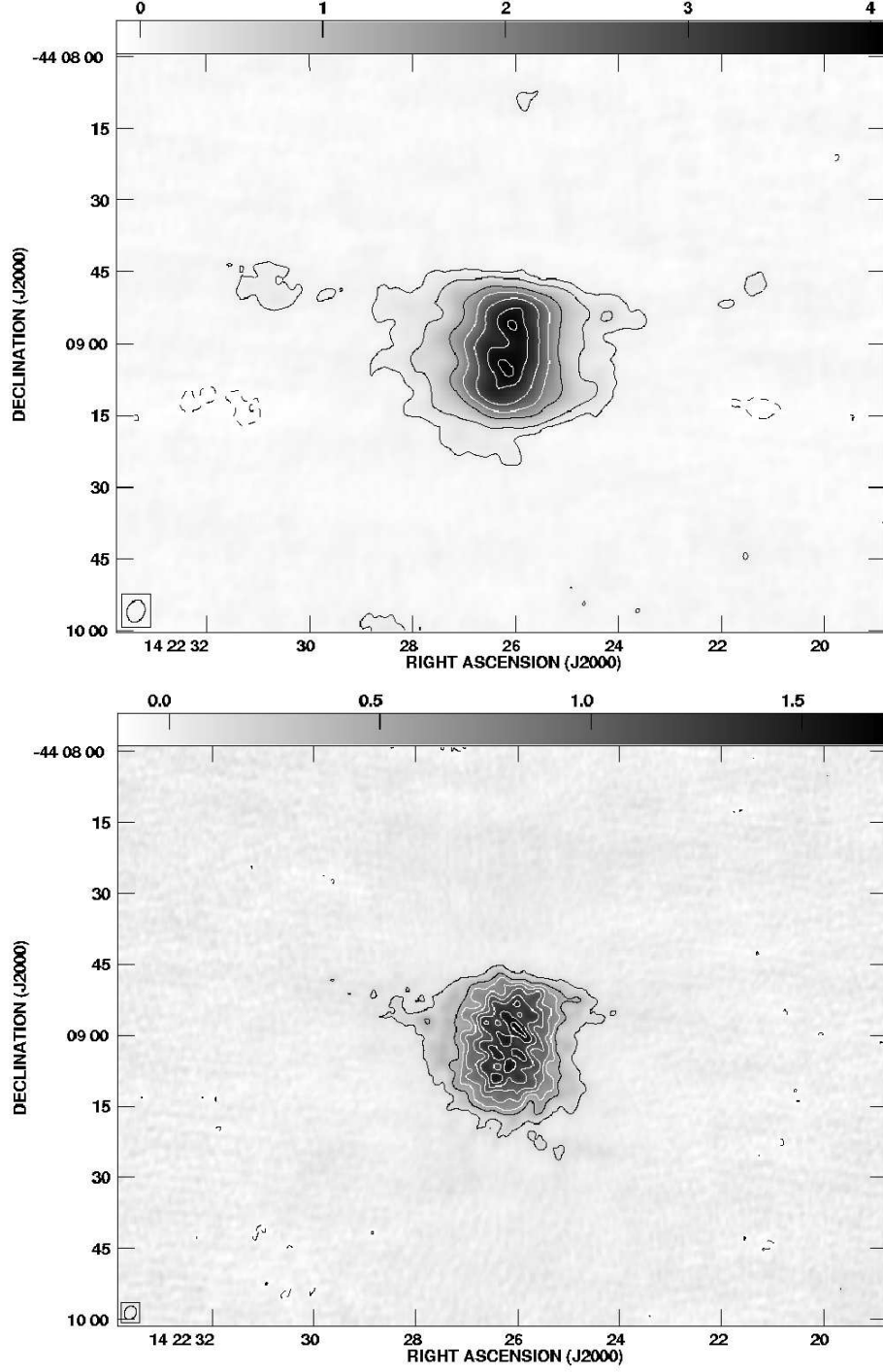


Fig. 1.— Radio maps of IC 4406 (*top*: 4.8 GHz, *bottom*: 8.6 GHz). The contours indicate the $(-3, 3, 10, 30, 50, 70, 90, 100)\sigma$ and the $(-3, 3, 10, 15, 20, 25, 30)\sigma$ levels for the top and bottom map respectively. Both maps were produced with NATURAL weights. The synthetic beam is shown in the bottom left of each map and the flux density unit is Jy/beam.

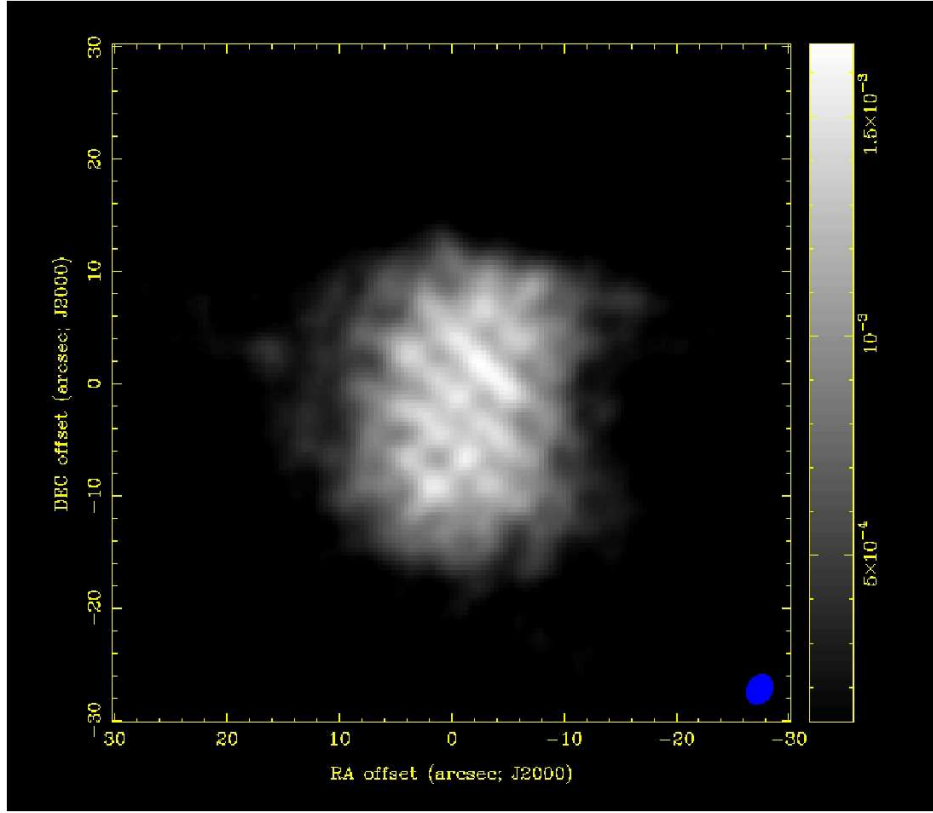


Fig. 2.— Greyscale image of the 8.6 GHz map. This map was obtained with NATURAL weighting, for a better sensitivity to weak structures. The flux density is in Jy/beam and the displayed values range from the 3σ to the peak level, which is 1.35 mJy/beam.

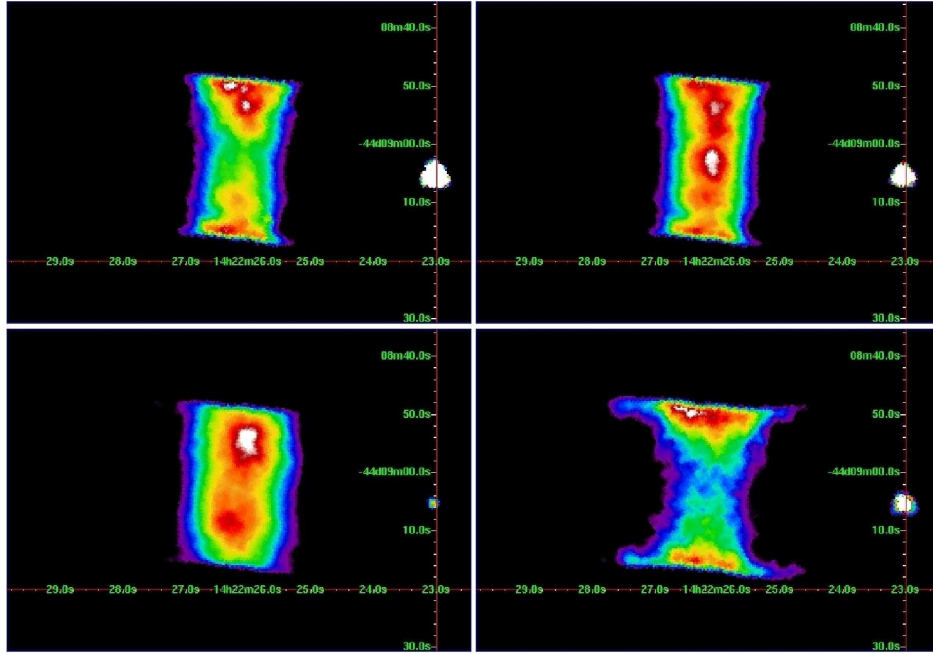


Fig. 3.— The central core emission observed with IRAC. The scale is linear: the maximum (white) is the emission peak in the area, the minimum (purple) is 50% of the maximum (maxima are respectively for 3.6, 4.5, 5.8 and 8.0 μm : 3.97, 5.85, 6.75 and 15.07 MJy/sr). Clockwise from top left: 3.6, 4.5, 5.8, 8.0 μm .

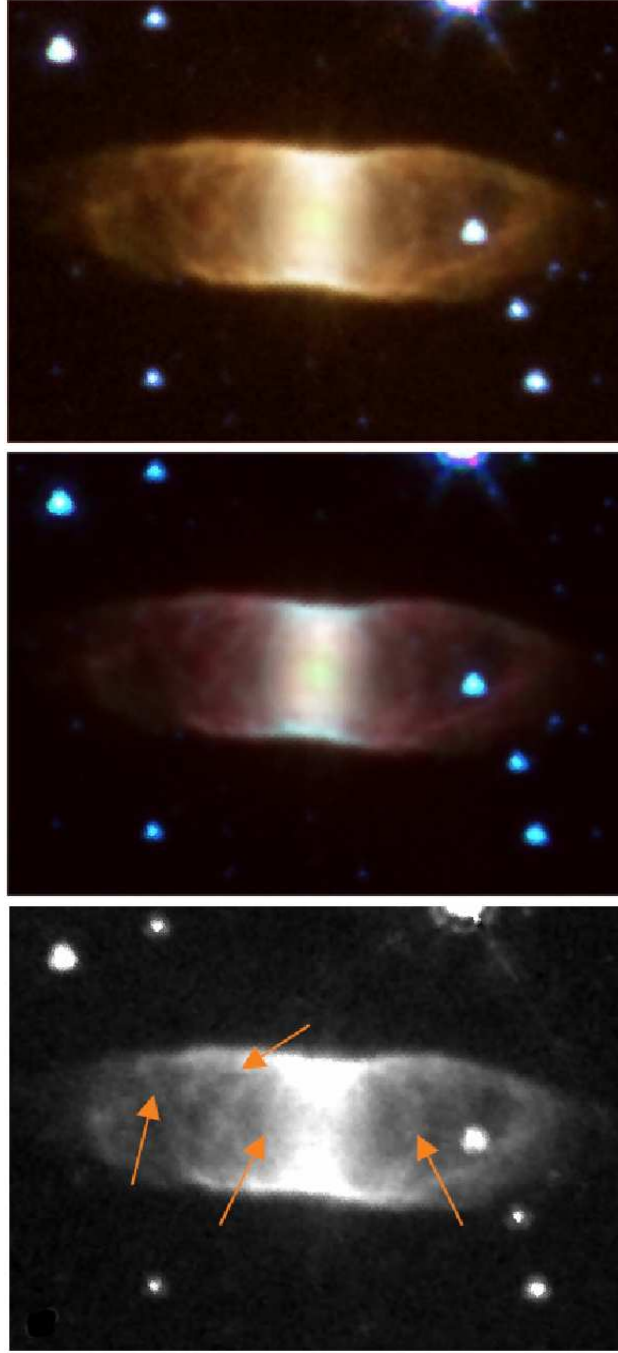


Fig. 4.— Images obtained with IRAC. *Top*: overlay of IRAC channels (blue is 3.6, green 4.5, orange 5.8 and red is 8.0 μm). *Middle*: as in the *top* image but not including 5.8 μm channel, for better viewing the central core emission. *Bottom*: 5.8 μm image scaled for a better view of the filament structures, some of which are pointed by the arrows.

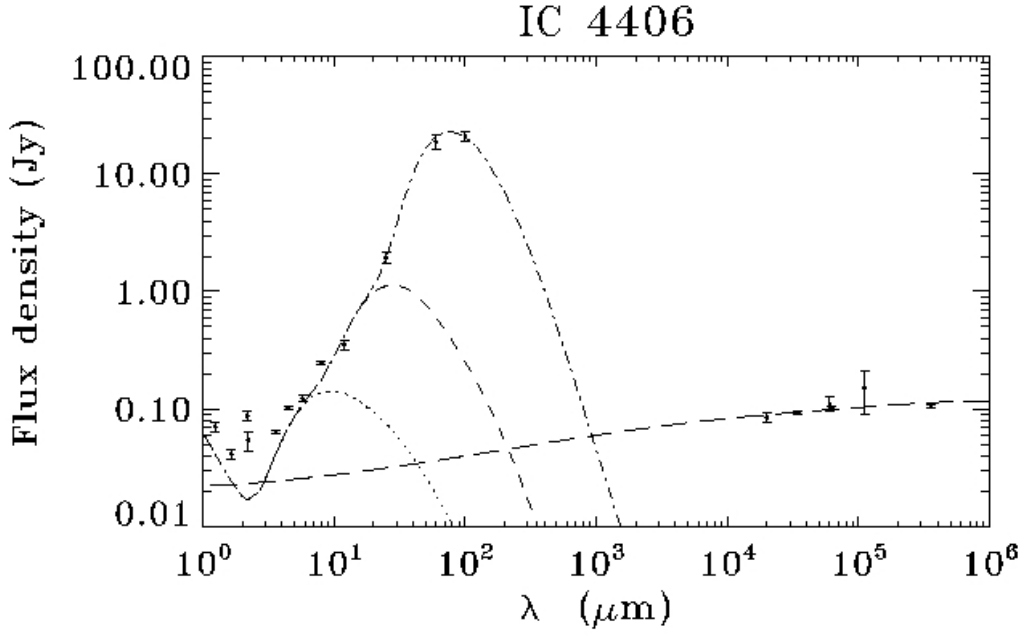


Fig. 5.— The single components in our best fit to the data are shown. The *dot* curve is the result of a model with the central star and the 700 K component, the *short dash* curve includes the central star, 700 K and 200 K components and the *dot-dash* curve includes the central star and the 700, 200, and 57 K dust components, the *long dash* curve is the free-free continuum.

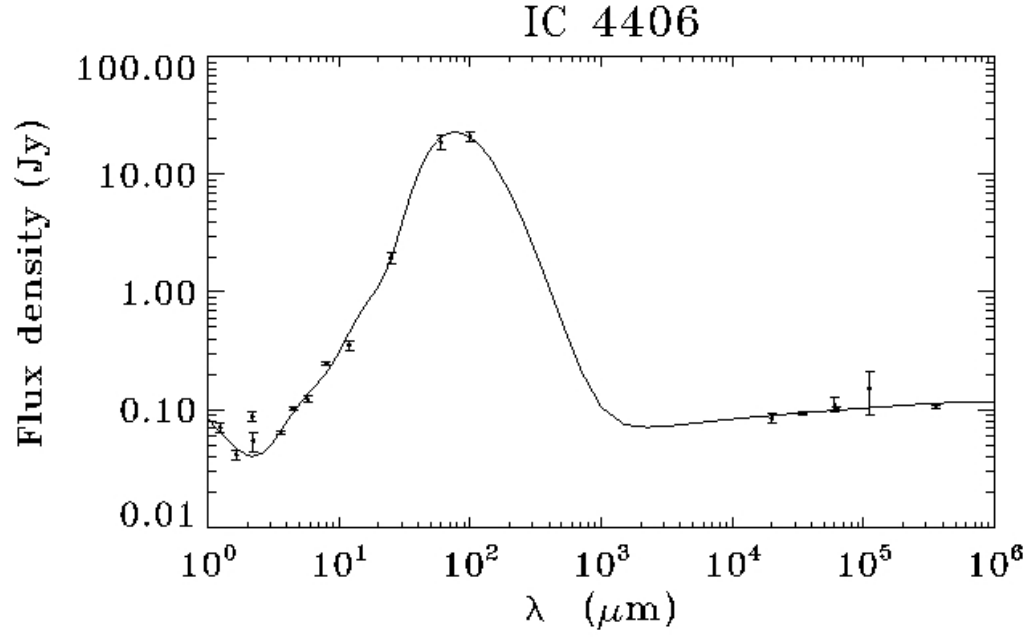


Fig. 6.— SED of IC 4406 from near-IR to radio wavelengths. The best fit is obtained summing the DUSTY and free-free continuum model outputs.

REFERENCES

- Cohen, M. and Barlow, M. J., 2005, MNRAS, 362, 1199
- Corradi, R. L. M., Perinotto, M., Schwarz, H. E. and Claeskens, J.-F., 1997, A&A, 322, 975
- Cox, P., Omont, A., Huggins, P. J., Bachiller, R. and Forveille, T., 1992, A&A, 266, 420
- Fazio, G. et al., 2004, ApJS, 154(1), 10
- Gathier, G. A., Pottasch, S. R. and Pel, J. W., 1986, A&A, 157, 171
- Gathier and Pottasch, S., 1988, A&A, 197, 226
- Gruenwald, R., Viegas, S. M. and Broguière, D., 1997, ApJ, 480, 283
- Hora, J. L., Latter, W. B., Allen, L. E., Marengo, M., Deutsch, L. K. and Pipher, J. L., 2004, ApJ, 154, 296
- Ivezić, Ž., Nenkova, M. and Elitzur, M., 1999, User Manual for DUSTY, Internal Report, Univ. of Kentucky, accessible at <http://www.pa.uky.edu/~moshe/dusty>
- Jura, M., 1986, ApJ, 303, 327
- Karzas, W. J. and Latter, R., 1961, ApJ, 6, 167
- Latter, W. B., Kelly, D. M., Hora, J. L. and Deutsch, L. K., 1995, ApJS, 100, 159
- Liu, X.-W., Barlow, M. J., Cohen, M., Danziger, I. J., Luo, S.-G., Baluteau, J. P., Cox, P., Emery, R. J., Lim, T. and Péquignot, D., 2001, MNRAS, 323, 343
- Mathis, J. S., Rumpl, W. and Nordsieck, K. H., 1977, ApJ, 217, 425
- Mauch, T., Murphy, T., Buttery, H. J., Curran, J., Hunstead, R. W., Piestrzynski, B., Robertson, J. G. and Sadler, E. M., 2003, MNRAS, 342(4), 1117
- Milne, D. K. and Aller, L. H., 1975, A&A, 38, 183
- Milne, D. K. and Aller, L. H., 1982, A&AS, 50, 209
- Milne, D. K. and Webster, B. L., 1979, A&AS, 36, 179
- O’Dell, C. R., Balick, B., Hajian, A. R., Henney, W. J. and Burkert, A., 2002, AJ, 123, 3329
- Phillips, J. P., 2003, MNRAS, 344(2), 501

- Phillips, J. P. and Ramos-Larios, G., 2005, MNRAS, 364(3), 849
- Pottasch, S., 1984, Planetary Nebulae - A Study of Late Stages of Stellar Evolution, D. Reidel Publishing Co., Dordrecht
- Pottasch, S. R., Baud, B., Beintema, D., Emerson, J., Habing, H. J., Harris, S., Houck, J., Jennings, R. and Marsden, P., 1984, A&A, 138, 10
- Ramos-Larios, G., Kemp, S. N. and Phillips, J. P., 2006, Rev. Mexicana Astron. Astrofis., 42, 131
- Sahai, R., Wooten, A., Schwarz, H. E. and Clegg, R. E. S., 1991, A&A, 251, 560
- Sarkar, G. and Sahai, R., 2006, ApJ, 644, 1171
- Schlegel, D., Finkbeiner, D. P. and Davis, M., 1998, ApJ, 500, 525
- Schuster, M. T., Marengo, M. and Patten, B., 2006, SPIE, 6270, 65
- Skrutskie, M. F., et al., 2006, AJ, 131, 1163
- Storey, J. W. V., 1984, MNRAS, 206, 521
- Wang, W., Liu, X.-W., Zhang, Y. and Barlow, M. J., 2004, A&A, 427, 873